

# Direct observational evidence that higher-luminosity type 1 active galactic nuclei are most commonly triggered by galaxy mergers

Yongmin Yoon<sup>1\*</sup>, Yongjung Kim<sup>2,3,\*\*</sup>, Dohyeong Kim<sup>4,\*\*\*</sup>, Kyungwon Chun<sup>5</sup>, and Woowon Byun<sup>5</sup>

<sup>1</sup> Department of Astronomy and Atmospheric Sciences, College of Natural Sciences, Kyungpook National University, Daegu 41566, Republic of Korea

<sup>2</sup> School of Liberal Studies, Sejong University, 209 Neungdong-ro, Gwangjin-Gu, Seoul 05006, Republic of Korea

<sup>3</sup> Department of Physics and Astronomy, Sejong University, 209 Neungdong-ro, Gwangjin-Gu, Seoul 05006, Republic of Korea

<sup>4</sup> Department of Earth Sciences, Pusan National University, Busan 46241, Republic of Korea

<sup>5</sup> Korea Astronomy and Space Science Institute (KASI), 776 Daedeokdae-ro, Yuseong-gu, Daejeon 34055, Republic of Korea

December 3, 2025

## ABSTRACT

We examine the connection between galaxy mergers and the triggering of active galactic nuclei (AGNs) using a sample of 614 type 1 AGNs at  $z < 0.07$ , along with a control sample of inactive galaxies matched to the AGNs for comparison. We used tidal features, detected in deep images from the DESI Legacy Imaging Survey, as direct evidence of recent mergers. We find that the fraction of type 1 AGN hosts with tidal features ( $f_T$ ) is higher for AGNs with higher luminosities and (to a lesser extent) more massive black holes. Specifically,  $f_T$  rapidly increases from  $0.05 \pm 0.03$  to  $0.75 \pm 0.13$  as the luminosity of the [O III]  $\lambda 5007$  emission line ( $L_{[\text{O III}]}$ ), an indicator for bolometric AGN luminosity, increases in the range  $10^{39.5} \lesssim L_{[\text{O III}]} / (\text{erg s}^{-1}) \lesssim 10^{42.5}$ . In addition,  $f_T$  increases from  $0.13 \pm 0.03$  to  $0.43 \pm 0.09$  as black hole mass ( $M_{\text{BH}}$ ) increases in the range  $10^{6.0} \lesssim M_{\text{BH}} / M_{\odot} \lesssim 10^{8.5}$ . The fraction  $f_T$  also increases with the Eddington ratio, although the trend is less significant compared to that with  $L_{[\text{O III}]}$  and  $M_{\text{BH}}$ . The excess of  $f_T$ , defined as the ratio of  $f_T$  for AGNs to that of their matched inactive counterparts, exhibits similar trends, primarily increasing with  $L_{[\text{O III}]}$  and weakly with  $M_{\text{BH}}$ . Our results indicate that, in the local Universe, galaxy mergers are the predominant triggering mechanism for high-luminosity AGNs, whereas they play a lesser role in triggering lower-luminosity AGNs. Additionally, strong events, such as galaxy mergers, may be more necessary to activate massive black holes in more massive galaxies due to their lower gas fractions.

**Key words.** galaxies: active – galaxies: interactions – quasars: general – quasars: supermassive black holes

## 1. Introduction

An active galactic nucleus (AGN) is a highly energetic region found at the center of a galaxy. The energy released by AGNs originates from a supermassive black hole (SMBH) surrounded by an accretion disk of gas and dust. As the material falls toward the SMBH, gravitational and frictional processes heat the disk, producing intense radiation, mainly in the ultraviolet to optical wavelength range. This radiation photoionizes gas on multiple spatial scales. The compact, high-density gas close to the SMBH ( $\lesssim 0.1$ – $1$  pc; Abuter et al. 2024) constitutes the broad-line region, where high bulk motion velocities broaden permitted lines to widths of several  $10^3$  km s<sup>-1</sup>. On larger scales (hundreds to thousands of parsecs; Schmitt et al. 2003), lower-density ionized gas forms the narrow-line region, which produces permitted and forbidden lines with typical widths of a few times  $10^2$  km s<sup>-1</sup>.

In type 1 AGNs, emission lines from both the broad- and narrow-line regions are visible, whereas in type 2 AGNs only the narrow emission lines are seen. According to the AGN unified model (Antonucci 1993; Urry & Padovani 1995), the difference between type 1 and type 2 arises from the line-of-sight viewing angle of the AGN structures. Additional emission, such as radio waves, can arise from jets launched by interactions between magnetic fields and the spinning SMBH (Blandford & Znajek

1977; Urry & Padovani 1995). Even in the absence of such luminous jets, AGNs can emit radio waves through various mechanisms, such as AGN-driven winds and free-free emission from photoionized gas (Panessa et al. 2019).

Active galactic nuclei are efficient tools for probing several key aspects of the Universe. Some AGNs are extremely luminous, with bolometric luminosities exceeding  $10^{46}$  erg s<sup>-1</sup>, allowing them to be detected at redshifts higher than 6 and enabling studies of the early Universe (Kim et al. 2015a, 2019, 2020; Jiang et al. 2016; Wang et al. 2021; Sacchi et al. 2022). Moreover, AGNs are optimum laboratories for examining physics under extreme gravitational and electromagnetic conditions (Dovčiak et al. 2004; Jovanović & Popović 2008; Blandford et al. 2019). In addition, AGNs provide insights into galaxy evolution, as they are expected to play a significant role in regulating star formation and the mass growth of galaxies (Di Matteo et al. 2005; Bower et al. 2006; Croton et al. 2006; Hopkins et al. 2008; Arjona-Gálvez et al. 2024) through powerful winds and jets. This coevolution between AGNs and their host galaxies is reflected in the remarkably tight correlations between SMBH mass and host galaxy properties (Di Matteo et al. 2005; Kormendy & Ho 2013).

Active galactic nuclei can be triggered through various channels. For instance, the supply of cold gas from hot halos of galaxy clusters, as well as ram pressure within clusters, can provide the necessary fuel for AGN activity (Gaspari et al. 2013; Li & Bryan 2014; Tremblay et al. 2016; Poggianti et al.

\* yyoona@knu.ac.kr

\*\* yongjungkim@sejong.ac.kr

\*\*\* dh.dr2kim@gmail.com

2017). Secular processes, including the influence of bars and disk instabilities, can also drive gas inflows that ignite AGNs (Shlosman et al. 1989; Crenshaw et al. 2003; Ohta et al. 2007; Hirschmann et al. 2012). In addition, galaxy mergers play an important role, as the induced tidal torques cause gas to lose angular momentum and flow toward the galaxy center, where accretion onto the SMBH can then power AGN activity (Di Matteo et al. 2005; Springel et al. 2005; Hopkins et al. 2008; Capelo et al. 2015).

Previous observational studies have attempted to determine whether galaxy mergers can trigger AGNs. Several studies have shown that AGNs are more likely to be found in interacting or post-merger galaxies compared to inactive galaxies (e.g., there is an excess of the merger fraction, suggesting that mergers can trigger AGN activity (Carpineti et al. 2012; Cotini et al. 2013; Ellison et al. 2013; Hong et al. 2015; Marian et al. 2020; Pierce et al. 2022; Araujo et al. 2023; Hernández-Toledo et al. 2023; Li et al. 2023; Comerford et al. 2024). Some studies have found that dust-obscured high-luminosity AGNs (Kim et al. 2015b, 2023, 2024a,b; Kim & Im 2018) are associated with galaxy mergers (Urrutia et al. 2008; Glikman et al. 2015). However, several studies found no evidence of the connection between mergers and AGNs (Gabor et al. 2009; Cisternas et al. 2011; Kocevski et al. 2012; Sabater et al. 2015; Mechtley et al. 2016; Villforth et al. 2014, 2017; Marian et al. 2019; Shah et al. 2020; Zhao et al. 2022). Furthermore, it has been found that higher-luminosity AGNs are most likely to be triggered by mergers (Treister et al. 2012; Ellison et al. 2013; Urbano-Mayorgas et al. 2019; Pierce et al. 2022, 2023; Hernández-Toledo et al. 2023; Tang et al. 2023; Euclid Collaboration et al. 2025), while other studies did not find such a trend (Villforth et al. 2014; Marian et al. 2020; Steffen et al. 2023; Comerford et al. 2024). Therefore, despite extensive examinations in numerous studies, the connection between galaxy mergers and AGN triggering, as well as its dependence on AGN luminosity, remains a controversial issue that has yet to be fully resolved.

In this study we aim to obtain a more definitive answer by investigating the problem using a large sample of type 1 AGNs and tidal features detected in deep images. While type 2 or other types of AGNs have been thoroughly examined in the previous studies, large samples of type 1 AGNs have not been widely used due to the challenges in sample selection, which requires sophisticated spectral fitting, and due to their bright unobscured AGN emission, which can hinder detailed investigation of the host galaxies. A major strength of using type 1 AGNs lies in their utility for probing essential AGN properties, such as black hole (BH) masses and Eddington ratios. Specifically, probing the Eddington ratio can reveal hidden but important aspects, as it can provide a more balanced perspective on how mergers influence BH activity by identifying low-mass BHs with low AGN luminosities but high Eddington ratios (e.g., Greene & Ho 2007), which are often blended with regularly accreting massive BHs.

Tidal features, which are remnants of stellar debris from galaxy mergers and can be detected through deep images (Quinn 1984; Barnes 1988; Hernquist & Spergel 1992; Feldmann et al. 2008), provide a powerful tool for studying the AGN–merger connection. Because they can persist for several gigayears after a merger, tidal features help overcome the limitation that observations capture only a snapshot of the Universe (Schweizer & Seitzer 1992; Tal et al. 2009; Kaviraj et al. 2011; Sheen et al. 2012, 2016; Duc et al. 2015; Yoon & Lim 2020; Yoon et al. 2022, 2023, 2024a,b; Bílek et al. 2023; Hernández-Toledo et al. 2023). Based on merger signatures de-

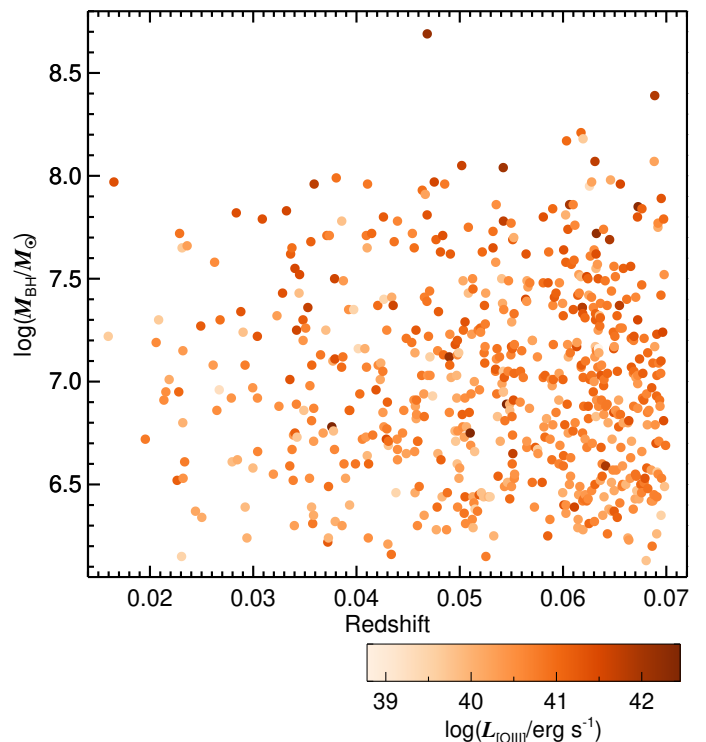


Fig. 1: Distributions of type 1 AGNs in the redshift vs.  $\log M_{\text{BH}}$  plane. Type 1 AGNs are indicated by colored circles, with the color representing  $\log L_{[\text{OIII}]}$ . See the color bar for the color scale.

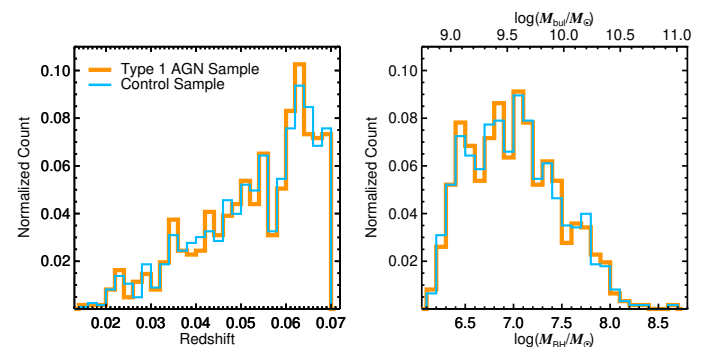


Fig. 2: Histograms of the normalized distributions of redshift and  $\log M_{\text{BH}}$  (or equivalently,  $\log M_{\text{bul}}$ ) for the type 1 AGN sample and the matched inactive control sample.

tected in deep images from the Dark Energy Spectroscopic Instrument (DESI) Legacy Imaging Survey (Dey et al. 2019), we examined whether galaxy mergers are a significant triggering mechanism of AGNs and, if so, which AGN properties are most closely associated with mergers, using a large sample of 614 type 1 AGNs at  $z < 0.07$ . By doing so, we offer a more definitive understanding of the relation between AGNs and galaxy mergers.

In this study, the cosmological parameters are taken to be  $H_0 = 70 \text{ km s}^{-1} \text{ Mpc}^{-1}$  for the Hubble constant,  $\Omega_\Lambda = 0.7$  for the dark energy density, and  $\Omega_m = 0.3$  for the matter density. The luminosity of the [O III]  $\lambda 5007$  emission line (or the bolometric AGN luminosity) is expressed in units of  $\text{erg s}^{-1}$ , and the BH mass in solar masses ( $M_\odot$ ).

Table 1: Properties of type 1 AGNs.

SDSS ObjID	R.A. <sup>a</sup>	decl. <sup>a</sup>	Redshift	$\log L_{[\text{O III}]}$ <sup>b</sup>	$\log L_{\text{bol}}$ <sup>c</sup>	$\log M_{\text{BH}}$ <sup>d</sup>	$\log \lambda_{\text{Edd}}$ <sup>e</sup>	Tidal feature <sup>f</sup>
587741727654543452	190.38112	26.04266	0.01596	39.70	43.25	7.22	-2.1	N
587739811560882185	214.49812	25.13687	0.01651	41.43	44.97	7.97	-1.1	Y
587725039018311737	180.30980	-3.67807	0.01955	40.84	44.39	6.72	-0.4	N
587733080809668634	171.40070	54.38255	0.02060	40.62	44.17	7.19	-1.1	Y
588017721176686710	169.03189	41.39811	0.02084	39.72	43.27	7.30	-2.1	N
587741489825775725	145.51997	23.68526	0.02135	40.60	44.15	6.91	-0.9	N
587742903405707293	203.02007	17.04897	0.02154	40.57	44.11	6.95	-0.9	N
587732771575955522	144.55110	7.72779	0.02186	40.16	43.70	7.01	-1.4	N
588023669707440191	181.12363	20.31630	0.02263	41.20	44.75	6.52	0.1	N
587729158970736727	204.56613	4.54259	0.02279	41.07	44.61	6.95	-0.4	Y
587738618103922723	182.68449	38.33619	0.02287	40.93	44.47	7.72	-1.4	N
587742061616037971	200.22362	21.91952	0.02306	39.56	43.10	6.15	-1.2	N
587739407321006093	190.43562	35.06277	0.02311	39.74	43.29	7.65	-2.5	N
587738616483282976	154.95622	33.36771	0.02318	40.05	43.59	6.80	-1.3	N
587726033846272089	150.52933	3.05769	0.02319	40.40	43.94	7.15	-1.3	N

**Notes.** The full table is available at the CDS.

<sup>(a)</sup> The units of R.A. and decl. are degrees. <sup>(b)</sup> The logarithmic luminosity of the [O III]  $\lambda 5007$  emission line.  $L_{[\text{O III}]}$  is expressed in units of  $\text{erg s}^{-1}$ . <sup>(c)</sup> The logarithmic bolometric luminosity of the AGN.  $L_{\text{bol}}$  is expressed in units of  $\text{erg s}^{-1}$  and is converted from  $L_{[\text{O III}]}$  using the relation  $L_{\text{bol}} \approx 3500 L_{[\text{O III}]}$  (Heckman et al. 2004). <sup>(d)</sup> The logarithmic BH mass.  $M_{\text{BH}}$  is expressed in solar masses ( $M_{\odot}$ ). <sup>(e)</sup> The logarithmic Eddington ratio. <sup>(f)</sup> The presence of tidal features in the host galaxy: Y = present, N=absent.

## 2. Sample

The sample of AGNs used in this study is from the catalog of type 1 AGNs from Oh et al. (2015). Oh et al. (2015) cataloged 5553 type 1 AGNs, including low-luminosity AGNs with weak broad-line regions, identified through the analysis of galaxy spectra in the Sloan Digital Sky Survey (SDSS) Data Release (DR) 7. The selection criteria for the type 1 AGNs are as follows: a redshift ( $z$ ) of  $< 0.2$ , a full width at half maximum (FWHM) of broad H $\alpha$  lines exceeding  $800 \text{ km s}^{-1}$ , and an amplitude-over-noise ratio<sup>1</sup> of broad H $\alpha$  lines higher than 3, along with additional criteria such as a completeness cut of  $> 90\%$  derived from simulations using mock spectra.

In this study we used type 1 AGNs at  $z < 0.07$ . This redshift cut represents a compromise between ensuring a statistically sufficient number of AGNs in the sample and avoiding higher-redshift AGN hosts, which are more likely to be affected by small angular sizes and the cosmological surface brightness dimming effects (see Eq. (6) in Yoon & Park 2020), making tidal feature detection more challenging. The initial sample includes 640 AGNs at  $z < 0.07$ . Of these, 26 AGNs are excluded due to their poor image quality mainly caused by proximity to bright sources (Sect. 3). Thus, the final sample for this study comprises 614 AGNs. We note that our results do not depend on redshift within the range we set ( $z < 0.07$ ), which we confirmed by dividing the sample into a couple of redshift bins and applying the same analysis, although the statistical significance is reduced due to the smaller sample sizes.

Here, the luminosity of the [O III]  $\lambda 5007$  emission line ( $L_{[\text{O III}]}$ ) is used as an indicator of AGN luminosity, as is commonly adopted in previous studies (Alonso et al. 2007; Oh et al. 2015; Ellison et al. 2013; Comerford et al. 2024).<sup>2</sup> We converted

$L_{[\text{O III}]}$  into the AGN bolometric luminosity ( $L_{\text{bol}}$ ) by using the correction relation of  $L_{\text{bol}} \approx 3500 L_{[\text{O III}]}$  (with a variance of 0.38 dex) from Heckman et al. (2004). As in Oh et al. (2015), we used BH masses ( $M_{\text{BH}}$ ) derived from the single-epoch mass estimation method developed by Greene & Ho (2005), which is based on the line width and luminosity of the broad H $\alpha$  emission estimated in Oh et al. (2015). The Eddington ratio ( $\lambda_{\text{Edd}}$ ) was defined as  $L_{\text{bol}}/L_{\text{Edd}}$ , where  $L_{\text{Edd}}$  is the Eddington luminosity, which is a function of  $M_{\text{BH}}$ . To illustrate the general properties of the AGNs, Fig. 1 displays the distributions of type 1 AGNs in the redshift versus  $\log M_{\text{BH}}$  plane, with the color of the circles indicating  $\log L_{[\text{O III}]}$  for the AGN sample. In Table 1 we present the properties of type 1 AGNs in our sample, including information on the presence of tidal features in their host galaxies.

The  $\log L_{[\text{O III}]}$  range of our AGN sample is above  $\sim 39.5$ , as a consequence of the AGN selection criteria used in the catalog of Oh et al. (2015). Together with other criteria, Oh et al. (2015) selected AGNs based on the signal strength of the broad H $\alpha$  line and a completeness cut, which is mainly determined by the broad H $\alpha$  line luminosity. Such criteria can result in a lower limit on  $L_{[\text{O III}]}$ , given its strong correlation with broad H $\alpha$  line luminosity (Spearman's rank correlation coefficient = 0.6).

For a quantitative comparison, we defined inactive control sample based on galaxies in SDSS. Previous studies commonly matched control sample based on redshift and mass (Marian et al. 2020; Araujo et al. 2023; Li et al. 2023; Tang et al. 2023; Avirett-Mackenzie et al. 2024; Byrne-Mamahit et al. 2024). According to McAlpine et al. (2020), including additional matching parameters beyond redshift and mass is not likely to be crucial, as the recovered results are not sensitive to the choice of matching criteria. In this study, the inactive galaxies in the control sample are matched to type 1 AGNs based on  $M_{\text{BH}}$  and redshift. For each AGN, we matched two inactive galaxies that either lack emission lines or exhibit only emission lines classified as star-forming<sup>3</sup> according

<sup>1</sup> It is defined as the ratio between the amplitude of the Gaussian-modeled emission line and the dispersion of the continuum residual.

<sup>2</sup> Our main findings are similarly obtained when using the luminosity of the broad H $\alpha$  emission as a proxy for AGN luminosity, instead of  $L_{[\text{O III}]}$ . However, to ensure consistency and facilitate comparison with other studies, we adopted  $L_{[\text{O III}]}$  as an indicator of AGN luminosity throughout this study.

<sup>3</sup> The emission line classification information is obtained from the Max Planck Institute for Astrophysics–Johns Hopkins Univer-

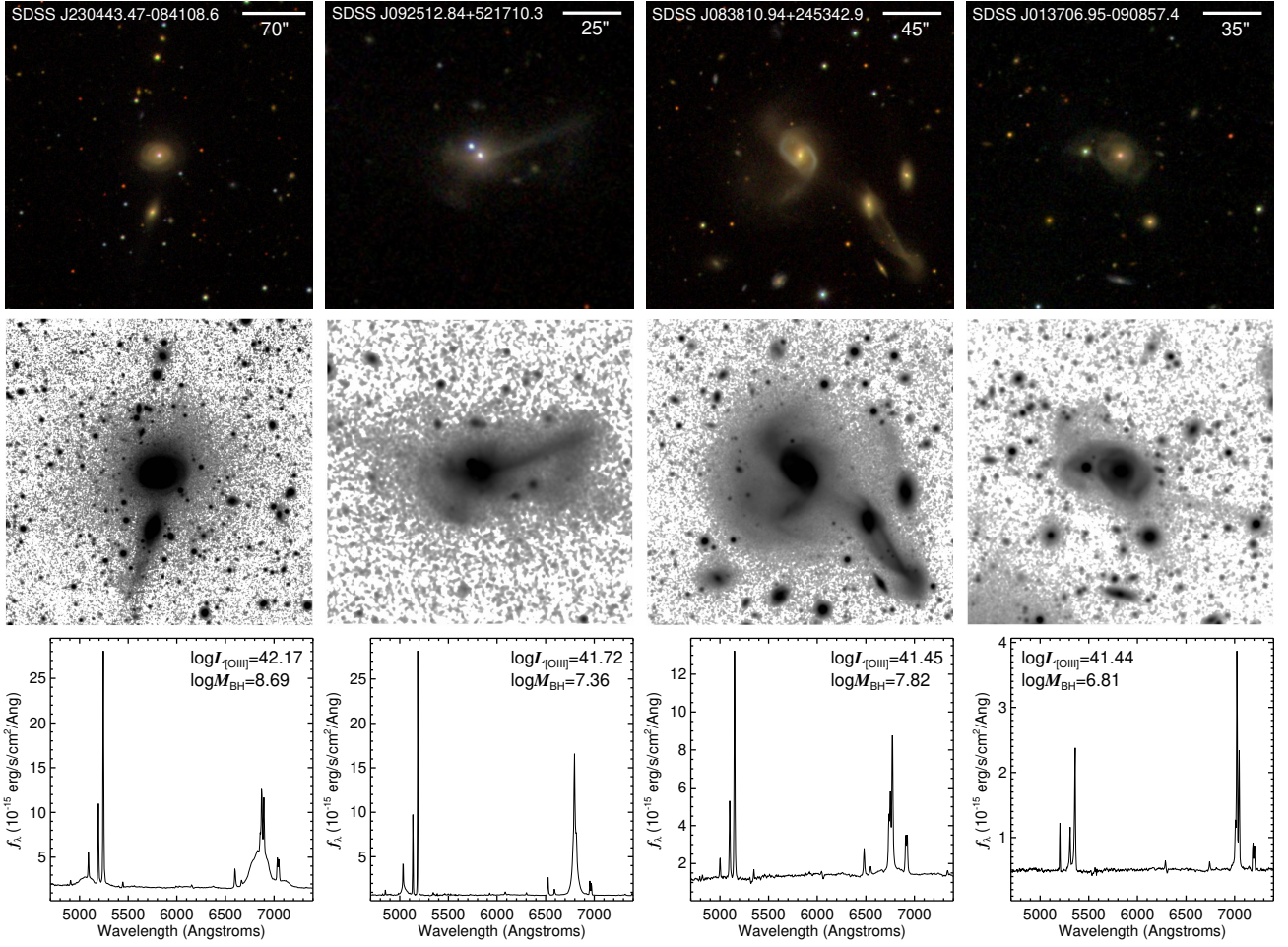


Fig. 3: Examples of type 1 AGN hosts with tidal features, which have  $\log(L_{[\text{O III}]}) > 41.4$ . First row: Color images from SDSS. The galaxy ID is provided. The horizontal bar indicates the angular scale of the image. Second row:  $r$ -band deep images of the DESI Legacy Imaging Survey. The angular scale of the deep image matches that of the color image in the first row. Third row: Optical spectra of type 1 AGNs covering the observed wavelength range 4700-7400Å, in which H $\beta$ , [O III], and H $\alpha$  emission lines are visible. Also shown are the values of  $\log L_{[\text{O III}]}$  and  $\log M_{\text{BH}}$ , where  $L_{[\text{O III}]}$  is in units of  $\text{erg s}^{-1}$  and  $M_{\text{BH}}$  is in units of solar mass ( $M_{\odot}$ ).

to the criterion of the Baldwin, Phillips, and Terlevich diagram (Baldwin et al. 1981), as defined by Kauffmann et al. (2003) and Brinchmann et al. (2004).

Applying the BH scaling relation between  $M_{\text{BH}}$  and  $M_{\text{bul}}$  presented by Kormendy & Ho (2013),<sup>4</sup> the  $M_{\text{BH}}$  values of inactive galaxies are derived from their bulge stellar masses ( $M_{\text{bul}}$ ), which are obtained from the Mendel et al. (2014) catalog. This catalog provides bulge, disk, and total stellar mass estimates based on the two-dimensional bulge+disk decompositions<sup>5</sup> performed by Simard et al. (2011). AGNs and inactive galaxies are matched within a redshift range of 0.002 and a  $M_{\text{BH}}$  range of  $\sim 0.1$  dex. The number of inactive galaxies in the control sample is 1228.

In Fig. 2 we compare the normalized distributions of redshift (left panel) and  $\log M_{\text{BH}}$  (right panel) for the type 1 AGN sample and their matched inactive control sample. The two sam-

ples show nearly identical distributions, as intended through the matching process.

Osborne & Salim (2024) evaluated the uncertainties and systematic errors in the bulge-to-total light ratios (based on the de Vaucouleurs plus exponential disk model) from Simard et al. (2011) catalog by comparing them with values derived from higher-resolution *Hubble* Space Telescope images. They reported a standard deviation of 0.2 and a median offset of 0.04 in the bulge-to-total light ratios, which implies that  $M_{\text{bul}}$  can be constrained with acceptable accuracy using SDSS images, despite their fundamental limitations. We note that the fraction of inactive galaxies with tidal features marginally increases with  $M_{\text{bul}}$  from  $0.07 \pm 0.01$  to  $0.10 \pm 0.02$  across the full 1.5 dex range of  $M_{\text{bul}}$  in our sample. Thus, the uncertainties and systematic errors in the estimation of  $M_{\text{bul}}$  have little effect on our main results.

### 3. Detection of tidal features

We used images from the DESI Legacy Survey DR10 (Dey et al. 2019) to detect tidal features. The DESI Legacy Survey com-

sity (MPA-JHU) catalog ([http://www.sdss.org/dr17/spectro/galaxy\\_mpajhu/](http://www.sdss.org/dr17/spectro/galaxy_mpajhu/)).

<sup>4</sup>  $M_{\text{BH}}/10^9 M_{\odot} = 0.49(M_{\text{bul}}/10^{11} M_{\odot})^{1.17}$

<sup>5</sup> The decompositions are conducted using the de Vaucouleurs plus exponential disk model.



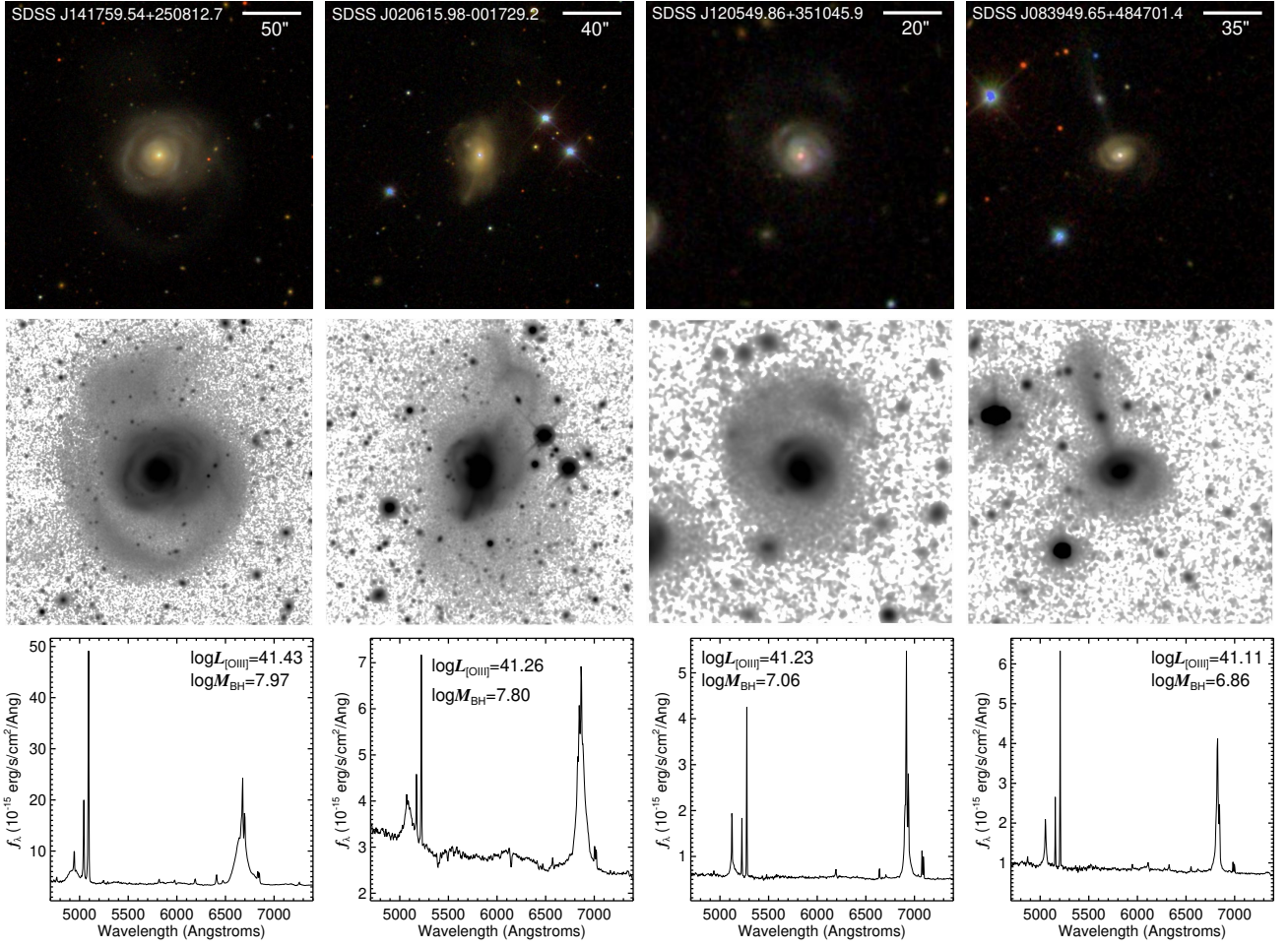


Fig. 4: Same as Fig. 3 but for  $41.1 < \log(L_{\text{OIII}}/\text{erg s}^{-1}) < 41.5$ .

prises three wide-area surveys: the Dark Energy Camera Legacy Survey, the Beijing–Arizona Sky Survey, and the Mayall  $z$ -band Legacy Survey. Together, these surveys cover a total area of approximately 14,000 square degrees. The  $g$ - and  $r$ -band images from the DESI Legacy Survey reach a median surface brightness limit of about 27 mag arcsec<sup>-2</sup>, as defined by the  $1\sigma$  background noise within a  $1'' \times 1''$  area. This surface brightness limit is similar to that of the deep co-added  $r$ -band images of the Stripe 82 region of SDSS (Yoon & Lim 2020; Yoon et al. 2022, 2023), which are commonly used to identify low surface brightness tidal features around galaxies (e.g., Kaviraj 2010; Schawinski et al. 2010; Hong et al. 2015).

Tidal features are identified through visual inspection of the  $g$ - and  $r$ -band images,<sup>6</sup> along with composite color images that combine the  $g$ ,  $r$ , and  $z$  bands. During the visual inspection of the images, we individually adjusted pixel value scales (e.g., contrast stretching) and applied Gaussian smoothing with different kernel sizes for all AGN hosts and inactive galaxies in order to enhance faint signals and better identify diffuse tidal features.

Tidal features typically take the form of streams, tails, and multiple shells (Duc et al. 2015; Mancillas et al. 2019; Bílek et al. 2020, 2023; Sola et al. 2022). Tidal streams are thin, elongated features that often appear as fine filaments and are typically linked to minor mergers. In certain cases, these streams

are directly connected to smaller companion galaxies. Tidal tails are broad, stretched features that clearly protrude from the host galaxies. These elongated stellar structures, which can form during major mergers, have a similar appearance to tidal streams but are wider and can even extend to the scale of the host galaxies. In some instances, however, tails and streams are not easily distinguishable from one another (Bílek et al. 2020; Sola et al. 2022). Tidal shells have the form of arc-like features with distinct, sharp boundaries. These arcs can either follow a common alignment or be randomly distributed around the host galaxy. Shells located farther from the galaxy tend to be more diffuse. Some galaxies display a combination of different types of tidal features. In this study, tidal tails, streams, and shells, around galaxies are collectively categorized as tidal features.<sup>7</sup>

We find that 109 out of 614 type 1 AGN hosts have tidal features (17.8%). Examples of SDSS color images and deep  $r$ -band DESI Legacy Survey images of type 1 AGN hosts with tidal features are shown in the first and second rows of Figs. 3–5, while those of type 1 AGN hosts that do not have tidal features are displayed in the first and second rows of Fig. 6. The third rows of these figures display optical spectra of type 1 AGNs covering the observed wavelength range 4700–7400 Å, in which H $\beta$ ,

<sup>6</sup> The image depth in the  $g$  and  $r$  bands is approximately 1 magnitude deeper than that in the  $z$  band.

<sup>7</sup> For instance, the AGN hosts in the first column of Fig. 3 and in the fourth column of Fig. 4 exhibit tidal streams. The AGN hosts in the first and third column of Fig. 4 show tidal tails. The AGN host in the fourth column of Fig. 5 has tidal shells.

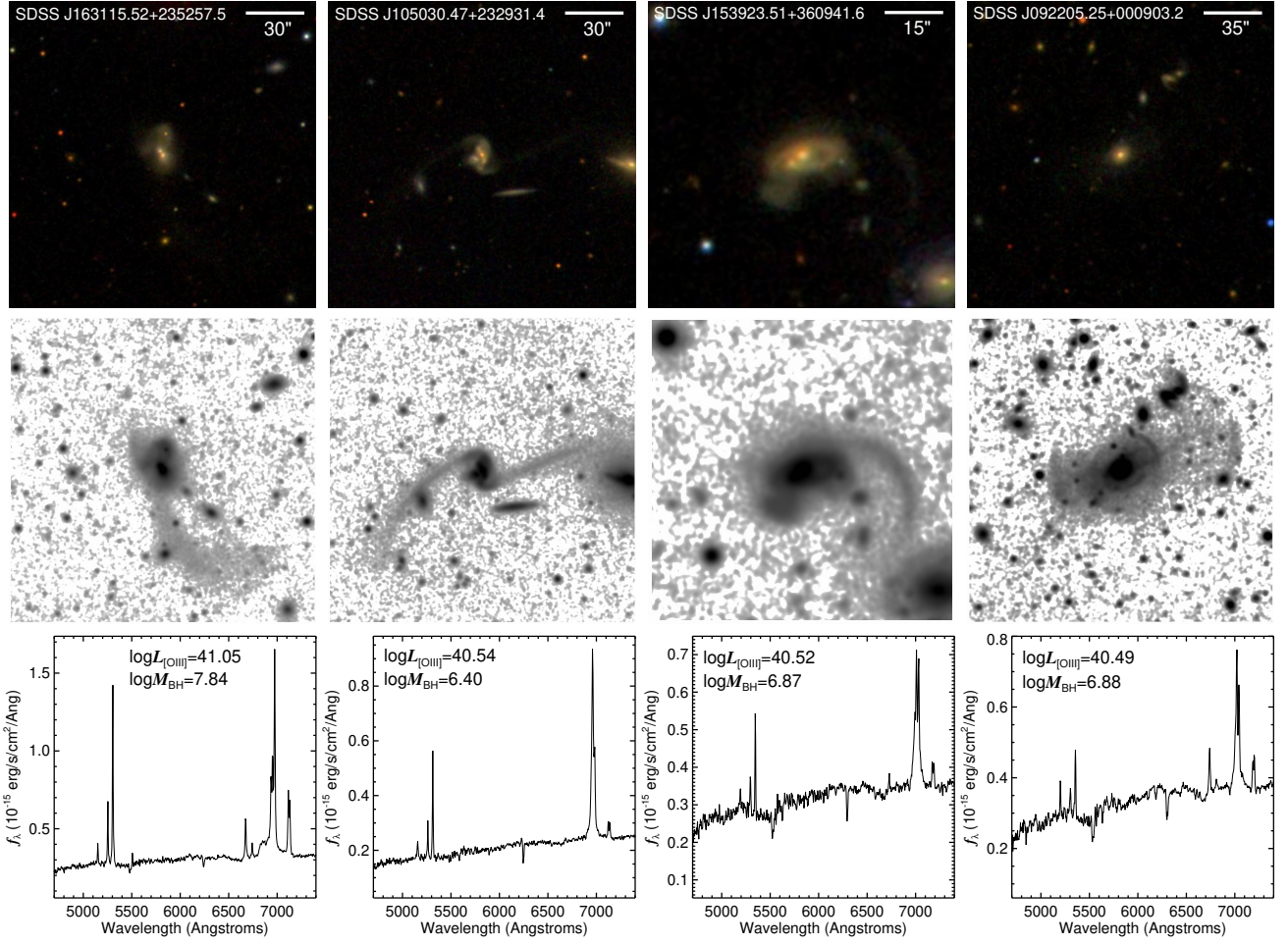


Fig. 5: Same as Fig. 3 but for  $40.4 < \log(L_{[\text{O III}]}) < 41.1$ .

[O III], and H $\alpha$  emission lines are visible. We also discover that 88 out of 1228 inactive galaxies in the control sample exhibit tidal features (7.2%).

We assessed the reliability of the tidal feature identification by comparing our primary classifications (performed by Y.Y.) with two independent classifications separately conducted by two authors (K.C. and W.B.) on a subsample of 262 type 1 AGNs with  $\log L_{[\text{O III}]} > 40.8$ . The comparison shows that 91% (62/68) and 87% (59/68) of AGN hosts identified as having tidal features by Y.Y. are also classified as having tidal features by K.C. and W.B., respectively. Additionally, 94% (183/194) and 97% (188/194) of AGN hosts without tidal features in Y.Y.'s classification are also identified as having no tidal features by K.C. and W.B., respectively. The outcome of this comparison indicates that the detection of tidal feature is highly consistent across different identifiers, even though it relies on visual inspection, which can be subjective. The high consensus rate over  $\sim 90\%$  for tidal feature identification is also found in our previous studies on the sample of early-type galaxies (Yoon & Lim 2020; Yoon et al. 2022, 2024b). The consensus rate of  $\sim 90\%$ – $95\%$  can introduce an additional potential uncertainty of  $\sim 0.01$ – $0.08$  to the fraction of tidal features presented in Sect. 4, depending on the number of samples per bin. We note that these uncertainties are smaller than the standard errors defined in this study.

#### 4. Results

We present the properties of our type 1 AGNs and their distributions in Figs. 7 and 8. Figure 7 displays the distribution of type 1 AGNs in the logarithmic values of  $M_{\text{BH}}$  versus  $L_{[\text{O III}]}$  (or  $L_{\text{bol}}$ ) plane, in which AGNs are divided based on the presence or absence of tidal features. Figure 8 shows histograms representing the distributions of  $\log L_{[\text{O III}]}$ ,  $\log M_{\text{BH}}$ , and  $\log \lambda_{\text{Edd}}$  for AGN hosts with and without tidal features.

Figure 7 shows that AGN hosts with tidal features are spread across the region in the  $\log M_{\text{BH}}$  versus  $\log L_{[\text{O III}]}$  plane that is populated by AGN hosts without tidal features. However, AGN hosts with tidal features are more likely to lie in the region of higher  $L_{[\text{O III}]}$  and higher  $M_{\text{BH}}$ , compared to those without tidal features.

Figure 8 demonstrates that type 1 AGN hosts with tidal features have median  $L_{[\text{O III}]}$  and  $M_{\text{BH}}$  values that are 0.28 and 0.22 dex higher, respectively, than those without tidal features. By conducting a Kolmogorov–Smirnov (KS) test on the two distributions of  $\log L_{[\text{O III}]}$  for the two AGN categories, we find that the probability ( $0 \leq p \leq 1$ ) of the null hypothesis, in which the two distributions stem from the same distribution, is  $p = 3.2 \times 10^{-5}$ . Similarly, a KS test on the two distributions of  $\log M_{\text{BH}}$  for the two AGN populations yields  $p = 6.2 \times 10^{-4}$ . Thus, these tests prove that AGN hosts with and without tidal features have significantly different distributions of  $L_{[\text{O III}]}$  and  $M_{\text{BH}}$ . AGN hosts with tidal features have a slightly higher median  $\log \lambda_{\text{Edd}}$ , by 0.08 dex,



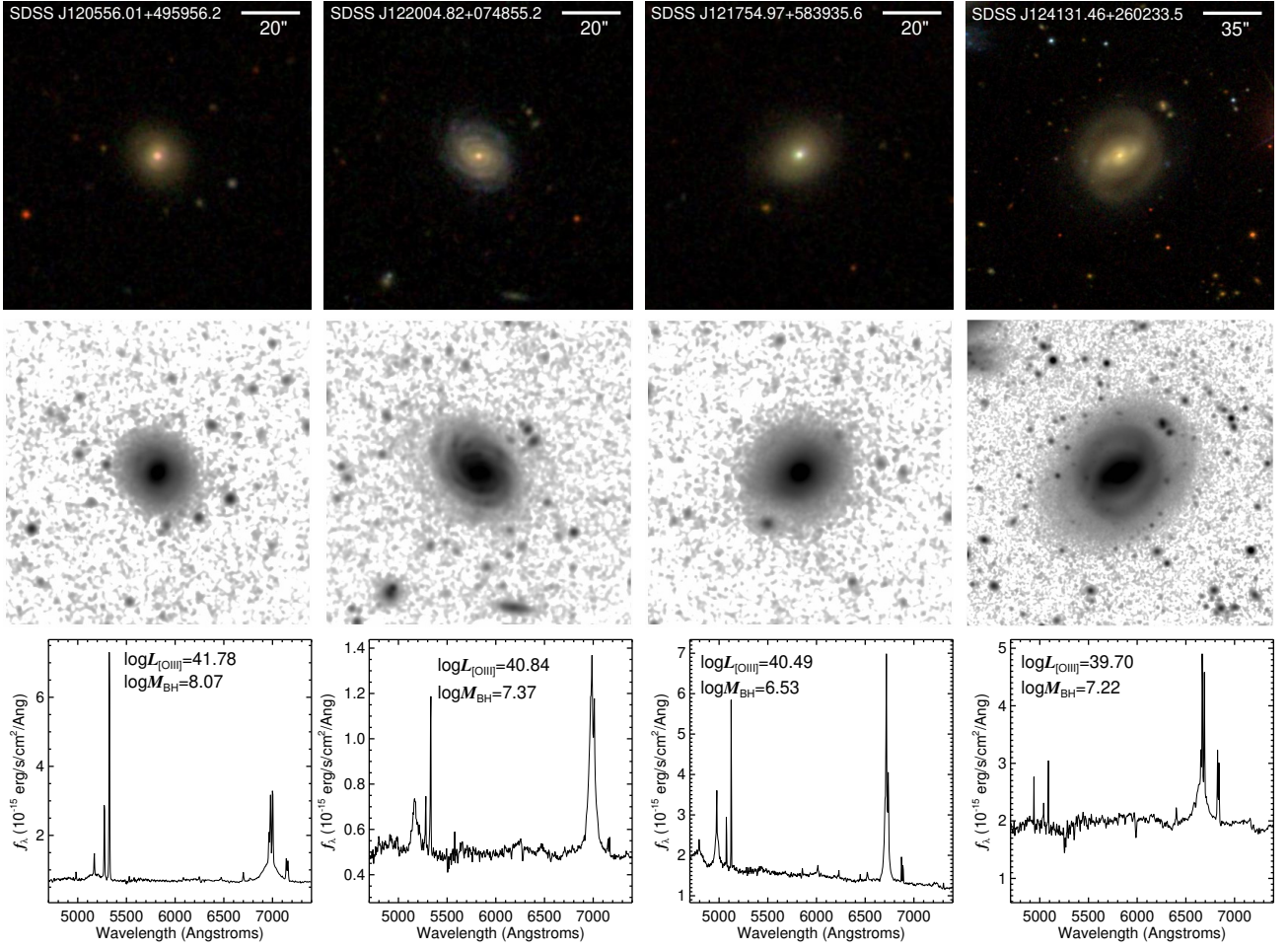


Fig. 6: Same as Fig. 3 but for type 1 AGN hosts that do not have tidal features. The AGNs are ordered by decreasing  $L_{[\text{O III}]}$  from left to right.

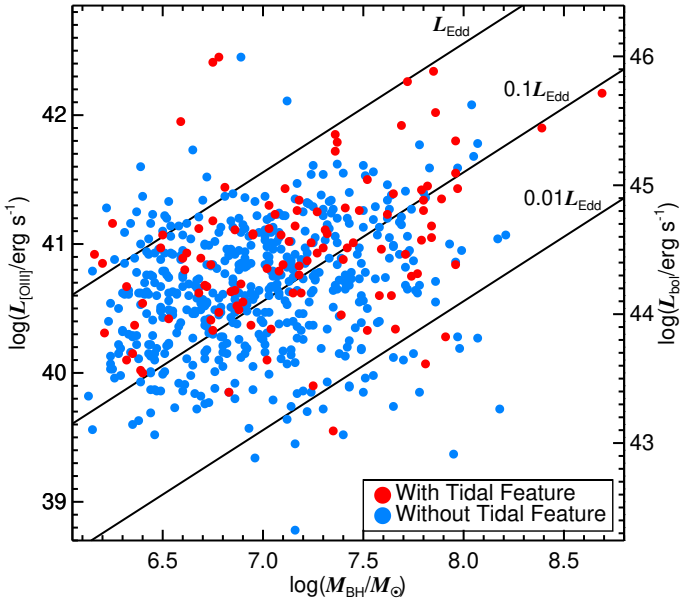


Fig. 7: Distribution of type 1 AGNs in the plane of logarithmic values of  $M_{\text{BH}}$  vs.  $L_{[\text{O III}]}$  (or  $L_{\text{bol}}$ ). AGNs are categorized according to the presence or absence of tidal features. The solid black lines indicate constant values of  $L_{\text{Edd}}$ ,  $0.1 L_{\text{Edd}}$ , and  $0.01 L_{\text{Edd}}$ .

than those without tidal features, but this difference is not statistically significant, as a KS test on the two distributions of  $\log \lambda_{\text{Edd}}$  for the two AGN categories yields  $p = 0.16$ . We reach the same conclusions by deriving  $p$ -values from Anderson–Darling tests conducted on the two distributions of  $\log L_{[\text{O III}]}$ ,  $\log M_{\text{BH}}$ , and  $\log \lambda_{\text{Edd}}$  for the two AGN categories. The tests yield  $p < 0.001$  for  $\log L_{[\text{O III}]}$  and  $\log M_{\text{BH}}$ , while for  $\log \lambda_{\text{Edd}}$ , the  $p$ -value is 0.13.

We display the fraction of type 1 AGN hosts with tidal features ( $f_T$ ) as a function of  $\log L_{[\text{O III}]}$ ,  $\log M_{\text{BH}}$ , and  $\log \lambda_{\text{Edd}}$  in the top panels of Fig. 9. The fraction  $f_T$  is defined as  $N_T/N_{\text{AGN}}$ , where  $N_{\text{AGN}}$  denotes the total number of AGN hosts, and  $N_T$  represents the number of AGN hosts with tidal features.<sup>8</sup> Figure 9 demonstrates a rapid increase in  $f_T$  with increasing  $L_{[\text{O III}]}$ , such that  $f_T$  for the lowest-luminosity AGNs with  $\log L_{[\text{O III}]} < 40.0$  is  $0.05 \pm 0.03$ , while for the highest-luminosity AGNs with  $\log L_{[\text{O III}]} > 41.9$ , it reaches  $0.75 \pm 0.13$ . We conducted a hypothesis test to compare the  $f_T$  values in the two extreme  $L_{[\text{O III}]}$  bins. The null hypothesis states that there is no difference between the  $f_T$  values of the highest- and lowest-luminosity AGNs, while the alternative hypothesis is that  $f_T$  of the highest-luminosity AGNs

<sup>8</sup> In this study, the uncertainties of  $f_T$  are given by the standard error of the proportion,  $\sqrt{f_T(1-f_T)/N_{\text{AGN}}}$ . These errors are nearly identical to those obtained from the bootstrapping method (resampling 2000 times for each bin), differing by no more than  $\sim 1$ –2%.

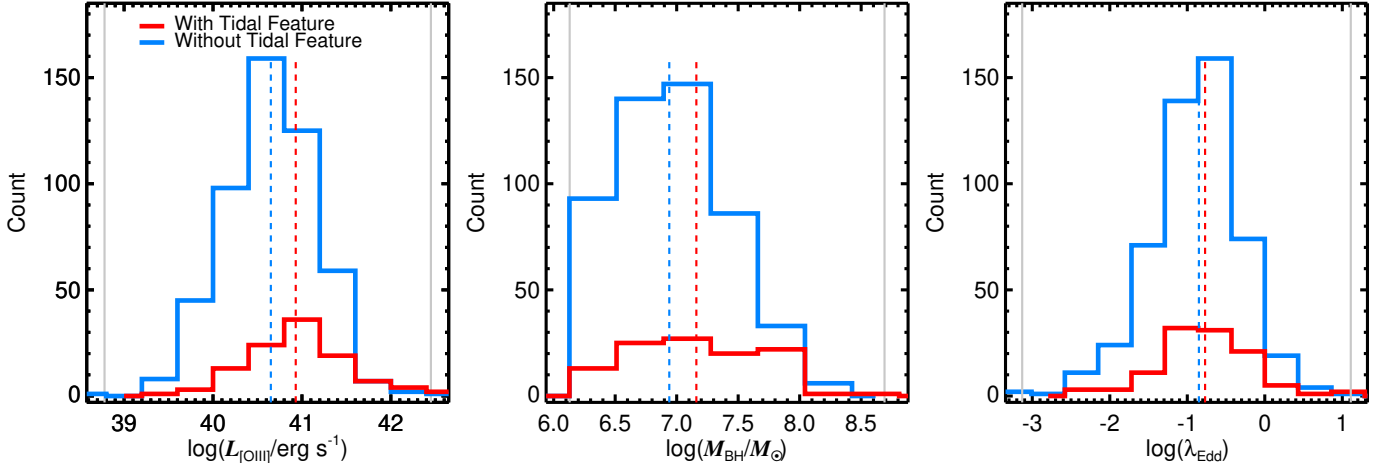


Fig. 8: Distributions of  $\log L_{\text{OIII}}$ ,  $\log M_{\text{BH}}$ , and  $\log \lambda_{\text{Edd}}$  for AGN hosts with and without tidal features. The vertical dashed lines represent the median value of each parameter for the two AGN categories. The gray vertical lines indicate the full range of each parameter.

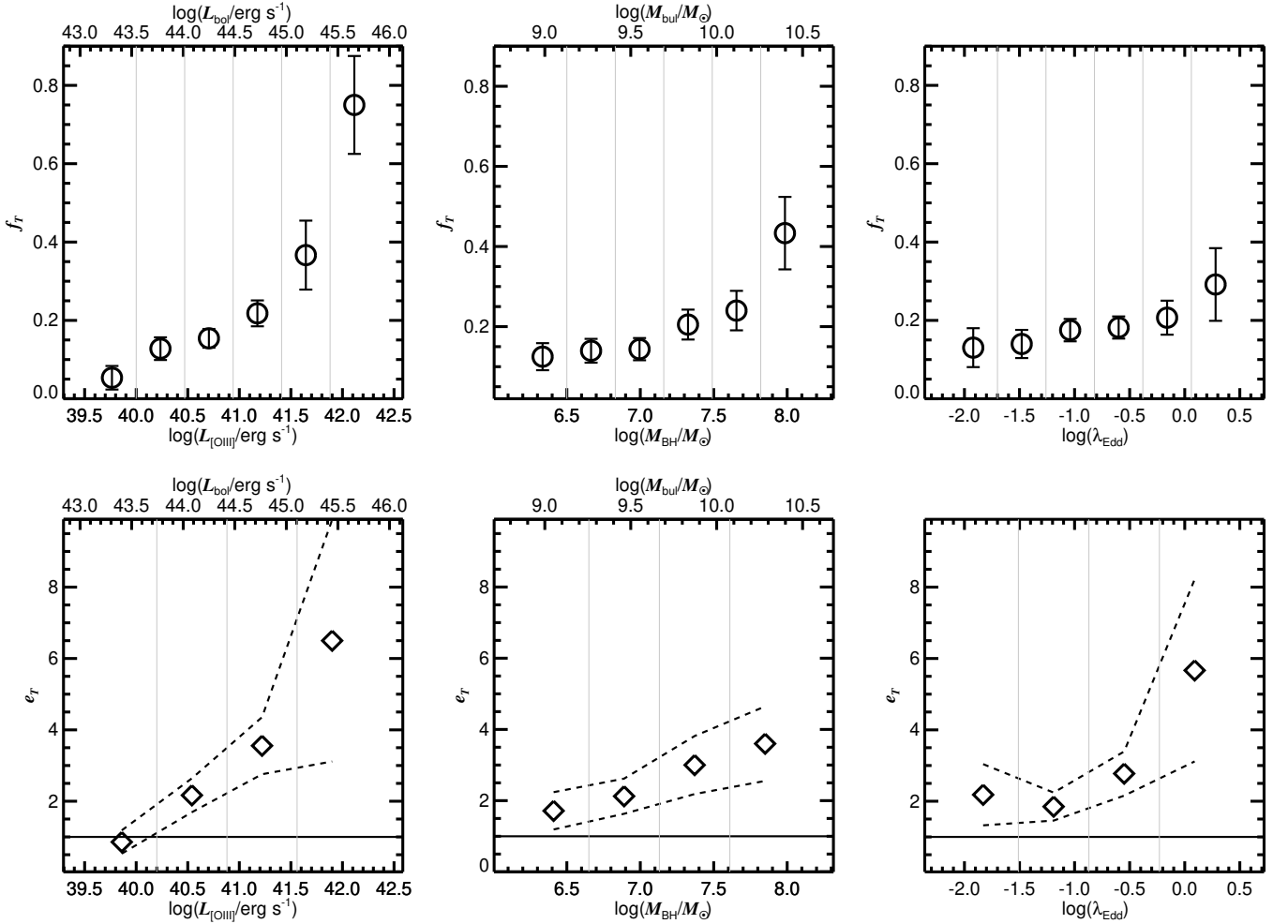


Fig. 9: Top panels: Fraction of type 1 AGN hosts with tidal features ( $f_T$ ) as a function of  $\log L_{\text{OIII}}$ ,  $\log M_{\text{BH}}$ , and  $\log \lambda_{\text{Edd}}$ . The error bar indicates the standard error of the proportion. Bottom panels: Excess of  $f_T$  ( $e_T$ ) as a function of  $\log L_{\text{OIII}}$ ,  $\log M_{\text{BH}}$ , and  $\log \lambda_{\text{Edd}}$ , defined as the ratio of  $f_T$  for AGNs to that of the matched inactive control sample. The dashed lines represent the range of the error value, computed through error propagation from the standard errors of the two proportions. The horizontal lines in the bottom panels represent  $e_T = 1$ , which indicates that the  $f_T$  of AGNs is identical to that of the inactive control sample. The gray vertical lines in all the panels mark the boundaries of the bins. The bin sizes in the bottom panels are set to be slightly larger (and hence there is a smaller number of bins) than those in the top panels, in order to reduce the larger uncertainties arising from the error propagation of the two proportion errors.



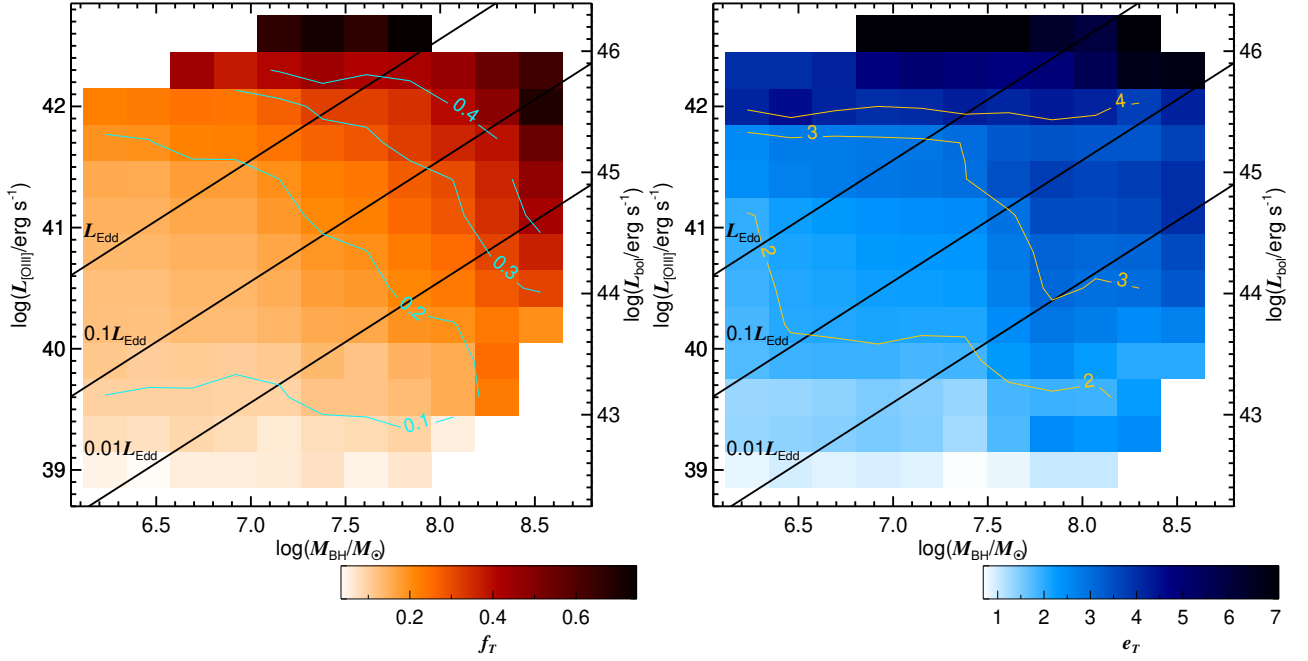


Fig. 10: Fraction of type 1 AGN hosts with tidal features ( $f_T$ ) and its excess ( $e_T$ ), defined as the ratio of  $f_T$  for AGNs to that of the matched inactive control sample, shown using colors and contours in the  $\log M_{\text{BH}}$  vs.  $\log L_{[\text{O III}]}$  plane (the left panel is for  $f_T$ , while the right panel is for  $e_T$ ). See the color bars for the color-coded representations of  $f_T$  and  $e_T$ . The values in the middle of the contour lines denote  $f_T$  or  $e_T$ . To create color maps and contours, we used a grid with block sizes of 0.23 dex and 0.30 dex along the  $\log M_{\text{BH}}$  and  $\log L_{[\text{O III}]}$  axes, respectively. At each grid point, we calculated  $f_T$  using a rectangular bin with side lengths of 1.38 dex and 1.80 dex along the  $\log M_{\text{BH}}$  and  $\log L_{[\text{O III}]}$  axes, respectively, and computed  $e_T$  using a rectangular bin with side lengths of 1.84 dex and 2.40 dex. Using a larger bin size than the grid block size to compute the parameters smooths the color maps and contours, revealing the large-scale trends more clearly. We display only the colored bins for which more than 10 and 25 AGNs are used to compute  $f_T$  and  $e_T$ , respectively.

is significantly higher than that of the low-luminosity AGNs. Using a one-tailed Z-test, we find a  $p$ -value of  $4.7 \times 10^{-9}$ . This implies that  $f_T$  of high-luminosity AGNs is significantly higher than that of low-luminosity AGNs.

Figure 9 also indicates that  $f_T$  increases with rising  $M_{\text{BH}}$ , as  $f_T$  for AGNs with  $\log M_{\text{BH}} < 6.5$  is  $0.13 \pm 0.03$ , while it is  $0.43 \pm 0.09$  for AGNs with  $\log M_{\text{BH}} > 7.8$ . For the  $f_T$  values in the two extreme  $M_{\text{BH}}$  bins, we performed a one-tailed hypothesis test, in which the null and the alternative hypotheses are of the same form as those described above. This test yields a  $p$ -value of  $1.1 \times 10^{-4}$ , suggesting that  $f_T$  of AGNs with high  $M_{\text{BH}}$  is significantly higher than that of AGNs with low  $M_{\text{BH}}$ .

The third column in the same figure shows that  $f_T$  also increases with  $\lambda_{\text{Edd}}$ , though the trend is weaker compared to those with  $L_{[\text{O III}]}$  and  $M_{\text{BH}}$ . Specifically,  $f_T$  for AGNs with  $\log \lambda_{\text{Edd}} < -1.7$  is  $0.13 \pm 0.05$ , while for AGNs with  $\log \lambda_{\text{Edd}} > 0.1$ , it is  $0.29 \pm 0.09$ . A one-tailed hypothesis test on the  $f_T$  values in the two extreme  $\lambda_{\text{Edd}}$  bins, with the null and the alternative hypotheses following the same structure as those described above, yields a  $p$ -value of 0.05. This suggests that the statistical significance of the trend, where  $f_T$  of AGNs with high  $\lambda_{\text{Edd}}$  is higher than that of AGNs with low  $\lambda_{\text{Edd}}$ , is relatively weak.

In the left panel of Fig. 10, we show  $f_T$  in the  $\log M_{\text{BH}}$  versus  $\log L_{[\text{O III}]}$  plane, in order to illustrate the composite trend of  $f_T$  with respect to  $L_{[\text{O III}]}$ ,  $M_{\text{BH}}$ , and  $\lambda_{\text{Edd}}$ .<sup>9</sup> This figure also

demonstrates that  $f_T$  is higher for AGNs with higher luminosities and more massive BHs, while it peaks at the highest-luminosity AGNs with  $\log L_{[\text{O III}]} \gtrsim 42$ , showing that the trend is more pronounced with AGN luminosity.

Lastly, we present the excess of  $f_T$  ( $e_T$ ) as a function of  $\log L_{[\text{O III}]}$ ,  $\log M_{\text{BH}}$ , and  $\log \lambda_{\text{Edd}}$  in the bottom panels of Fig. 9. The parameter  $e_T$  is defined as the ratio of  $f_T$  for AGNs in a given bin to that of their matched inactive control galaxies. Figure 9 shows that  $e_T$  increases from  $0.9 \pm 0.3$  to  $6.5 \pm 3.4$  as  $L_{[\text{O III}]}$  rises, indicating that  $f_T$  for low-luminosity AGNs is nearly identical to that of the matched inactive galaxies, whereas high-luminosity AGNs are more than six times as likely to exhibit tidal features as their inactive counterparts. Figure 9 also displays that  $e_T$  increases from  $1.7 \pm 0.5$  to  $3.6 \pm 1.0$  with rising  $M_{\text{BH}}$ , although the trend is weaker than that with  $L_{[\text{O III}]}$ . For  $\lambda_{\text{Edd}}$ ,  $e_T$  also increases with  $\lambda_{\text{Edd}}$ . At  $\log \lambda_{\text{Edd}} < -0.2$ , the rate of increase in  $e_T$  is modest (from  $\sim 2$  to 3). However, at very high Eddington ratios of  $\log \lambda_{\text{Edd}} > -0.2$ ,  $e_T$  rises sharply to  $5.7 \pm 2.6$ . Based on these results, we find that a certain level of excess in  $f_T$  exists across all AGNs, except for those with the lowest luminosities.

In the right panel of Fig. 10,  $e_T$  is shown in the  $\log M_{\text{BH}}$  versus  $\log L_{[\text{O III}]}$  plane, which displays how  $e_T$  varies jointly with  $L_{[\text{O III}]}$ ,  $M_{\text{BH}}$ , and  $\lambda_{\text{Edd}}$ . The figure illustrates that  $e_T$  primarily increases with AGN luminosity, with a weaker trend suggesting that AGNs with more massive BHs also exhibit higher  $e_T$ . The highest-luminosity AGNs with  $\log L_{[\text{O III}]} \gtrsim 42$  exhibit high values of  $e_T \gtrsim 4$  across all  $M_{\text{BH}}$ , including those with low  $M_{\text{BH}}$ , which correspond to AGNs with very high  $\lambda_{\text{Edd}}$ . This explains the sharp increase in  $e_T$  at very high  $\lambda_{\text{Edd}}$  shown in Fig. 9.

<sup>9</sup> We use larger bin sizes than the grid block size in Fig. 10 to smooth the color maps and contours, enhancing the visibility of large-scale trends. Therefore, for accurate values of  $f_T$  or  $e_T$  in a specific bin, it is recommended to refer to Fig. 9.

## 5. Discussion

### 5.1. Connection between AGNs and galaxy mergers

Our key result is that  $f_T$  and  $e_T$  are higher for more luminous AGNs, with  $f_T$  and  $e_T$  reaching 0.75 and  $\sim 6.5$ , respectively, for the highest-luminosity AGNs with  $\log L_{[\text{O III}]}\gtrsim 42$ . If  $f_T$  for AGNs can be interpreted as the fraction of AGNs triggered by mergers, this provides direct observational evidence that galaxy mergers are the predominant triggering mechanism for such high-luminosity AGNs. In addition, the progenitor galaxies involved in mergers that trigger high-luminosity AGNs are likely to be rich in gas (Byrne-Mamahit et al. 2023; Avirett-Mackenzie et al. 2024), as sustaining high-luminosity AGN radiation requires substantial gas accretion onto the BH (Byrne-Mamahit et al. 2023).

The fraction  $f_T$  of the lowest-luminosity AGNs with  $\log L_{[\text{O III}]}\lesssim 40$  is very low (0.05) and does not significantly differ from that of their inactive counterparts. This suggests that such low-luminosity AGNs are unlikely to be triggered by galaxy mergers; instead, other mechanisms mentioned in Sect. 1 may be responsible for their triggering. For instance, according to Hirschmann et al. (2012), disk instabilities can serve as a trigger mechanism for low- to moderate-luminosity AGNs with  $\log L_{\text{bol}}\lesssim 45$  (equivalent to  $\log L_{[\text{O III}]}\lesssim 41.5$ ) in the low-redshift Universe. Given that bar-driven fueling of central SMBHs has been observed in Seyfert galaxies (Crenshaw et al. 2003; Ohta et al. 2007), which host moderate-luminosity AGNs, bars can also trigger low- to moderate-luminosity AGNs with  $\log L_{\text{bol}}\lesssim 45$ . Ram pressure in cluster environments can trigger low-luminosity AGNs, as supported by the sample in Poggianti et al. (2017), in which AGN hosts experiencing ram pressure typically have  $\log L_{[\text{O III}]}\lesssim 41$ .

According to Durret et al. (2021), who studied 40 galaxy cluster samples,  $\sim 10\%$  of galaxies in clusters are experiencing ram pressure. This fraction can therefore be considered an upper limit to the population of ram-pressure-triggered AGNs in rich environments such as clusters, under the crude assumption that ram pressure is a highly effective AGN triggering mechanism. We matched our AGN sample to the large redshift-survey group catalog of Tempel et al. (2014), which is constructed from SDSS DR10. Among the 538 matched AGNs, we find that 58% of AGNs reside in group or cluster environments, while 13% are located in richer environments with  $\geq 10$  spectroscopic members, a typical threshold in observational work used to distinguish environments denser than poor clusters or rich groups (Miller et al. 2005; Porter & Raychaudhury 2005). Combining these figures, we estimate that roughly  $\lesssim 1\text{--}5\%$  of our AGN sample may be undergoing ram pressure. Future studies of AGN environments using large survey data will provide a more reliable estimate of the fraction of ram-pressure-triggered AGNs.

The other AGNs, except those in the highest- and lowest-luminosity bins, do not exhibit  $f_T$  higher than 0.4 but show the excess in  $f_T$  compared to their inactive counterparts. This implies that galaxy mergers contribute to triggering of these AGNs, although mergers are not the dominant triggering mechanism. Low- to moderate luminosity AGN populations are far more numerous than high-luminosity AGNs, which are primarily triggered by mergers. Therefore, it can be said that most AGNs are generally triggered by mechanisms other than galaxy mergers, as suggested by several studies (Treister et al. 2012; Steinborn et al. 2018; Man et al. 2019; McAlpine et al. 2020; Hernández-Toledo et al. 2023).

Since more massive galaxies tend to host more massive SMBH (Kormendy & Ho 2013), our finding that  $f_T$  is higher for

AGNs with higher  $M_{\text{BH}}$  is consistent with the previous studies showing that more massive galaxies are more likely to exhibit tidal features, suggesting a higher likelihood of recent mergers in more massive galaxies (Hong et al. 2015; Yoon & Lim 2020; Yoon et al. 2024a). However, the rate of increase in  $f_T$  with  $M_{\text{BH}}$  is higher for AGNs than for their inactive counterparts, as  $e_T$  is higher at higher  $M_{\text{BH}}$ . Although this trend is not very strong, it implies that galaxy mergers play a more crucial role in activating more massive SMBHs, as shown in the simulation by Hopkins et al. (2014). This trend may be related to the fact that lower-mass galaxies have a higher gas fraction (Hopkins et al. 2009; Masters et al. 2012). In this case, due to the abundant gas in lower-mass galaxies, mild mechanisms, other than mergers, can sufficiently induce gas inflow onto their SMBHs. In contrast, a stronger event, such as galaxy mergers, is more necessary to activate massive SMBHs in more massive galaxies due to their lower gas fraction, leading to increased  $e_T$  with increasing  $M_{\text{BH}}$ .

According to Pierce et al. (2023), the surface brightness depth of images is an important factor in studying merger features. Thus, our results may be affected by image depth. For example, a lot of very faint tidal features, which are only detectable through far deeper images, may be hidden around low-luminosity AGN hosts, meaning that the actual  $f_T$  for those AGNs could be much higher. Even if that is the case, we can still conclude that tidal features prominent enough to be detected in this study are more frequently found around AGNs with higher luminosities and more massive  $M_{\text{BH}}$ , which means that these AGNs are more likely associated with more significant or recent mergers than their low-luminosity or less massive counterparts. Moreover, the excess  $e_T$  is unlikely to be significantly influenced by image depth, as demonstrated by Ellison et al. (2019).

### 5.2. Near- and super-Eddington AGNs and the uncertainties in Eddington ratios

In our AGN sample, 5% have  $\lambda_{\text{Edd}}$  higher than 1. The large uncertainty associated with observed Eddington ratios may result in AGNs with intrinsically high Eddington ratios being identified as near- or super-Eddington AGNs. This uncertainty arises from several factors. Specifically, the conversion from  $L_{[\text{O III}]}$  to  $L_{\text{bol}}$  may involve an uncertainty larger than  $\sim 0.4$  dex (Heckman et al. 2004). Additionally, BH mass measurements based on single-epoch spectra are known to have uncertainties of a factor of 3 (Greene & Ho 2005). Combined, these factors can result in uncertainties of  $\sim 0.7$  dex in the Eddington ratios calculated in this study.

Another source of uncertainty that can lead to high observed Eddington ratios is the presence of narrow-line Seyfert 1 galaxies, whose broad emission lines have FWHMs of less than  $\sim 2000 \text{ km s}^{-1}$ . According to Marconi et al. (2008),  $M_{\text{BH}}$  values for this type of AGN can be underestimated by more than  $\sim 0.5$  dex, potentially contributing to the apparent excess of super-Eddington AGNs. However, excluding AGNs with FWHMs of broad H $\alpha$  lines below  $2000 \text{ km s}^{-1}$  (which account for 9% of our AGN sample) does not change our results, suggesting that the bias introduced by this effect is negligible.

However, it is also possible that some of the observed super-Eddington AGNs are genuinely accreting at such high rates. The structure of real AGNs often deviates significantly from the assumption of spherical symmetry used in calculating Eddington ratios, allowing for super-Eddington accretion to be physically possible in certain cases (Du et al. 2015). Taken together, while measurement uncertainties and potential narrow-line Seyfert 1

galaxies can inflate Eddington ratios, departures from spherical symmetry suggest that some objects are genuinely near- or super-Eddington. Accordingly, the Eddington ratios presented here should be interpreted with caution.

### 5.3. Comparison with previous studies

As mentioned earlier in Sect. 1, the excess of the merger fraction in AGN hosts is a controversial issue, but we find the direct evidence of a strong AGN–merger connection, particularly for very luminous AGNs. This demonstrates the importance of including AGNs with a wide range of luminosities in the sample to develop a comprehensive understanding of the AGN–merger connection. Redshift ranges of AGN samples can also be an important factor contributing to the different results, as most studies that found no evidence of a connection between mergers and AGNs use samples at higher redshifts ( $0.5 \lesssim z \lesssim 3.0$ ; Gabor et al. 2009; Cisternas et al. 2011; Kocevski et al. 2012; Mechtley et al. 2016; Villforth et al. 2014, 2017; Marian et al. 2019; Shah et al. 2020), while those suggesting the AGN–merger connection, including this study, typically focus on lower redshifts ( $z \lesssim 0.2$ ; Carpineti et al. 2012; Cotini et al. 2013; Ellison et al. 2013; Hong et al. 2015; Marian et al. 2020; Araujo et al. 2023; Hernández-Toledo et al. 2023; Li et al. 2023; Comerford et al. 2024). The difference in results due to the redshift range of the sample may stem from the fact that mergers play an increasingly important role in triggering AGNs as the Universe evolves, even though the abundance of merging systems decreases with decreasing redshift (McAlpine et al. 2020). In addition, the difficulty in detecting merger or disturbance features in high-redshift galaxies, due to cosmological surface brightness dimming and small angular sizes, may have influenced studies of high-redshift AGNs, as cosmological dimming has been identified as one of the most important factors affecting the study of merger features, according to Pierce et al. (2023).

Comparing our results with previous studies supporting the AGN–merger connection allows us to broaden our understanding of the general AGN population, as our analysis here is limited to type 1 AGNs selected through spectroscopy. Using type 2 AGNs with  $40.5 \lesssim \log L_{[\text{O III}]}$   $\lesssim 42.5$ , which overlaps with the luminosity range of our sample, Pierce et al. (2022) and Pierce et al. (2023) show that type 2 AGN hosts exhibit a substantially enhanced rate of morphological disturbance, by a factor of  $\sim 2$ – $3$ , compared with a matched control sample. Furthermore, the disturbance rate increases from 30% to 70% across the full luminosity range, accompanied by an increase in the enhancement factor relative to the control sample from 1 to 3. These findings are highly consistent with our results. Urbano-Mayorgas et al. (2019) suggest that low-luminosity type 2 AGNs with  $\log L_{[\text{O III}]} \lesssim 41.9$  exhibit a low fraction of disturbed morphology (6%) compared to high-luminosity type 2 AGNs with  $\log L_{[\text{O III}]} \gtrsim 41.9$ , which show a fraction of 34%. In addition, several previous studies support the AGN–merger connection for type 2 AGNs (Carpinetti et al. 2012; Araujo et al. 2023; Li et al. 2023).

Several studies based on type 1 AGNs report results consistent with ours. For instance, Urrutia et al. (2008) found that over  $\sim 80\%$  of intrinsically bright type 1 AGNs exhibit strong evidence of recent or ongoing mergers, based on dust-reddened quasars. Tang et al. (2023) reported a correlation between  $L_{\text{bol}}$  and host asymmetry in type 1 AGNs, which strengthens significantly at the highest luminosities of  $\log L_{\text{bol}} > 45$ . Similarly,

Hernández-Toledo et al. (2023) found that both type 1 and type 2 AGNs show a higher incidence of tidal features than a non-AGN control sample. Given that the difference between type 1 and type 2 AGNs arises from the viewing angle, according to the AGN unified model, it is reasonable that the AGN–merger connection and its luminosity-dependent trend are similarly observed in both types.

Multiple previous studies based on AGNs selected via X-ray or infrared observations are also consistent with our results, supporting the AGN–merger connection. For example, using an AGN sample selected from X-ray, infrared, and spectroscopic surveys, Treister et al. (2012) find a strong correlation between AGN luminosity and the fraction of host galaxies undergoing mergers. Specifically, the fraction increases from  $\sim 4\%$  at  $\log L_{\text{bol}} \sim 43$  to  $\sim 80\%$  at  $\log L_{\text{bol}} \sim 46$ , which is very similar to our result. Other studies also support the AGN–merger connection based on AGNs selected via X-ray or infrared (e.g., Cotini et al. 2013; Li et al. 2023). Thus, these results, combined with ours, imply that the AGN–merger connection, particularly for high-luminosity AGNs, can be identified across AGN samples selected through various wavelength windows.

## 6. Summary

Using a large sample of 614 type 1 AGNs at  $z < 0.07$ , we explored whether galaxy mergers are a significant triggering mechanism for AGNs and identified the AGN properties most associated with mergers, aiming to gain a clearer understanding of the AGN–galaxy merger connection. For the quantitative comparison, we used a control sample of inactive galaxies that are matched to AGNs by  $M_{\text{BH}}$  and redshift. We identified tidal features, which are direct evidence of recent mergers, through visual inspection of DESI Legacy Survey images with a surface brightness depth of  $\sim 27$  mag arcsec $^{-2}$ , a level that previous studies have shown to be sufficient for the detection of tidal features (Kaviraj 2010; Schawinski et al. 2010; Hong et al. 2015). We focused on two parameters: the fraction of type 1 AGN hosts with tidal features ( $f_T$ ) and its excess ( $e_T$ ), which is defined as the ratio of  $f_T$  for AGNs to that of the matched inactive control sample.

We discover that  $f_T$  is higher for AGNs with higher luminosities and (to a lesser extent) more massive BHs. Specifically,  $f_T$  rapidly increases from  $0.05 \pm 0.03$  to  $0.75 \pm 0.13$  as  $L_{[\text{O III}]}$  rises in the range  $10^{39.5} \lesssim L_{[\text{O III}]} / (\text{erg s}^{-1}) \lesssim 10^{42.5}$ , while  $f_T$  increases from  $0.13 \pm 0.03$  to  $0.43 \pm 0.09$  as  $M_{\text{BH}}$  increases in the range  $10^{6.0} \lesssim M_{\text{BH}} / M_{\odot} \lesssim 10^{8.5}$ . The fraction  $f_T$  also increases with  $\lambda_{\text{Edd}}$ , though the trend is less significant compared to those with  $L_{[\text{O III}]}$  and  $M_{\text{BH}}$ .

We also find that  $e_T$  primarily increases with AGN luminosity, with a weaker trend indicating that  $e_T$  is higher for AGNs with more massive BHs. Specifically,  $e_T$  increases from  $0.9 \pm 0.3$  to  $6.5 \pm 3.4$  as  $L_{[\text{O III}]}$  rises, where as  $e_T$  increases from  $1.7 \pm 0.5$  to  $3.6 \pm 1.0$  with increasing  $M_{\text{BH}}$ .

Our findings offer direct observational evidence that, in the local Universe, galaxy mergers are the predominant triggering mechanism for high-luminosity AGNs, whereas they play a lesser role in the triggering of lower-luminosity AGNs. In addition, our result suggest that a strong event, such as galaxy mergers, is more necessary to activate massive SMBHs in more massive galaxies because of their lower gas fractions.

With deeper images from future large surveys, we will classify tidal features into several types and explore how different types of mergers relate to AGN properties, as each tidal



feature type reflects mergers with distinct natures and origins (Yoon et al. 2024b).

## 7. Data availability

Table 1 is available at the CDS via <https://cdsarc.cds.unistra.fr/viz-bin/cat/J/A+A/vol/page>.

**Acknowledgements.** This research was supported by Kyungpook National University Research Fund, 2025. This research was supported by the National Research Foundation of Korea (NRF) grant funded by the Korea government (MSIT) (RS-2025-16064514). Y. K. was supported by the faculty research fund of Sejong University in 2025 and the National Research Foundation of Korea (NRF) grant funded by the Korean government (MSIT) (No. 2021R1C1C2091550). D.K. acknowledges the support by the National Research Foundation of Korea (NRF) grant (No. 2021R1C1C1C1013580) funded by the Korean government (MSIT). W.B. was supported by the Korea Astronomy and Space Science Institute under the R&D program (Project No. 2025-1-831-00) supervised by the Ministry of Science and ICT.

## References

- Abuter, R., Allouche, F., Amorim, A., et al. 2024, *Nature*, 627, 8003, 281
- Alonso, M. S., Lambas, D. G., Tissera, P., et al. 2007, *MNRAS*, 375, 1017
- Antonucci, R. 1993, *ARA&A*, 31, 473
- Araujo, B. L. C., Storch-Bergmann, T., Rembold, S. B., et al. 2023, *MNRAS*, 522, 5165
- Arjona-Gálvez, E., Di Cintio, A., & Grand, R. J. J. 2024, *A&A*, 690, A286
- Avirett-Mackenzie, M. S., Villforth, C., Huertas-Company, M., et al. 2024, *MNRAS*, 528, 6915
- Baldwin, J. A., Phillips, M. M., & Terlevich, R. 1981, *PASP*, 93, 5
- Barnes, J. E. 1988, *ApJ*, 331, 699
- Bílek, M., Duc, P.-A., Cuillandre, J.-C., et al. 2020, *MNRAS*, 498, 2138
- Bílek, M., Duc, P.-A., & Sola, E. 2023, *A&A*, 672, A27
- Blandford, R., Meier, D., & Readhead, A. 2019, *ARA&A*, 57, 467
- Blandford, R. D. & Znajek, R. L. 1977, *MNRAS*, 179, 433
- Bower, R. G., Benson, A. J., Malbon, R., et al. 2006, *MNRAS*, 370, 645
- Brinchmann, J., Charlot, S., White, S. D. M., et al. 2004, *MNRAS*, 351, 1151
- Byrne-Mamahit, S., Hani, M. H., Ellison, S. L., et al. 2023, *MNRAS*, 519, 4966
- Byrne-Mamahit, S., Patton, D. R., Ellison, S. L., et al. 2024, *MNRAS*, 528, 5864
- Capelo, P. R., Volonteri, M., Dotti, M., et al. 2015, *MNRAS*, 447, 2123
- Carpinetti, A., Kaviraj, S., Darg, D., et al. 2012, *MNRAS*, 420, 2139
- Choi, Y.-Y., Han, D.-H., & Kim, S. S. 2010, *Journal of Korean Astronomical Society*, 43, 191
- Cisternas, M., Jahnke, K., Inskip, K. J., et al. 2011, *ApJ*, 726, 57
- Comerford, J. M., Nevin, R., Negus, J., et al. 2024, *ApJ*, 963, 53
- Cotini, S., Ripamonti, E., Caccianiga, A., et al. 2013, *MNRAS*, 431, 2661
- Crenshaw, D. M., Kraemer, S. B., & Gabel, J. R. 2003, *AJ*, 126, 1690
- Croton, D. J., Springel, V., White, S. D. M., et al. 2006, *MNRAS*, 365, 11
- Dey, A., Schlegel, D. J., Lang, D., et al. 2019, *AJ*, 157, 168
- Di Matteo, T., Springel, V., & Hernquist, L. 2005, *Nature*, 433, 604
- Dovčiak, M., Karas, V., & Matt, G. 2004, *MNRAS*, 355, 1005
- Du, P., Hu, C., Lu, K.-X., et al. 2015, *ApJ*, 806, 1, 22
- Duc, P.-A., Cuillandre, J.-C., Karabal, E., et al. 2015, *MNRAS*, 446, 120
- Durret, F., Chiche, S., Lobo, C., et al. 2021, *A&A*, 648, A63
- Ellison, S. L., Mendel, J. T., Patton, D. R., et al. 2013, *MNRAS*, 435, 3627
- Ellison, S. L., Viswanathan, A., Patton, D. R., et al. 2019, *MNRAS*, 487, 2491
- Euclid Collaboration, La Marca, A., Wang, L., et al. 2025, *arXiv:2503.15317*
- Feldmann, R., Mayer, L., & Carollo, C. M. 2008, *ApJ*, 684, 1062
- Gabor, J. M., Impey, C. D., Jahnke, K., et al. 2009, *ApJ*, 691, 705
- Gaspari, M., Ruszkowski, M., & Oh, S. P. 2013, *MNRAS*, 432, 4, 3401
- Glikman, E., Simmons, B., Mailly, M., et al. 2015, *ApJ*, 806, 218
- Greene, J. E. & Ho, L. C. 2005, *ApJ*, 630, 122
- Greene, J. E. & Ho, L. C. 2007, *ApJ*, 670, 92
- Heckman, T. M., Kauffmann, G., Brinchmann, J., et al. 2004, *ApJ*, 613, 109
- Hernández-Toledo, H. M., Cortes-Suárez, E., Vázquez-Mata, J. A., et al. 2023, *MNRAS*, 523, 4164
- Hernquist, L. & Spitzer, D. N. 1992, *ApJ*, 399, L117
- Hirschmann, M., Somerville, R. S., Naab, T., et al. 2012, *MNRAS*, 426, 237
- Hong, J., Im, M., Kim, M., et al. 2015, *ApJ*, 804, 34
- Hopkins, P. F., Hernquist, L., Cox, T. J., et al. 2008, *ApJS*, 175, 356
- Hopkins, P. F., Kocovski, D. D., & Bundy, K. 2014, *MNRAS*, 445, 823
- Hopkins, P. F., Somerville, R. S., Cox, T. J., et al. 2009, *MNRAS*, 397, 802
- Jiang, L., McGreer, I. D., Fan, X., et al. 2016, *ApJ*, 833, 222
- Jovanović, P. & Popović, L. Č. 2008, *Fortschritte der Physik*, 56, 456
- Kauffmann, G., Heckman, T. M., Tremonti, C., et al. 2003, *MNRAS*, 346, 1055
- Kaviraj, S. 2010, *MNRAS*, 406, 382
- Kaviraj, S., Tan, K.-M., Ellis, R. S., et al. 2011, *MNRAS*, 411, 2148
- Kim, D. & Im, M. 2018, *A&A*, 610, A31
- Kim, D., Im, M., Glikman, E., et al. 2015b, *ApJ*, 812, 66
- Kim, Y., Im, M., Jeon, Y., et al. 2015a, *ApJ*, 813, L35
- Kim, Y., Im, M., Jeon, Y., et al. 2019, *ApJ*, 870, 86
- Kim, Y., Im, M., Jeon, Y., et al. 2020, *ApJ*, 904, 111
- Kim, D., Im, M., Kim, M., et al. 2023, *ApJ*, 954, 156
- Kim, D., Im, M., Lim, G., et al. 2024a, *Journal of Korean Astronomical Society*, 57, 95
- Kim, D., Kim, Y., Im, M., et al. 2024b, *A&A*, 690, A283
- Kocevski, D. D., Faber, S. M., Mozena, M., et al. 2012, *ApJ*, 744, 148
- Kormendy, J. & Ho, L. C. 2013, *ARA&A*, 51, 511
- Li, Y. & Bryan, G. L. 2014, *ApJ*, 789, 153
- Li, W., Nair, P., Irwin, J., et al. 2023, *ApJ*, 944, 168
- Man, Z.-yi., Peng, Y.-jie., Kong, X., et al. 2019, *MNRAS*, 488, 89
- Mancillas, B., Duc, P.-A., Combes, F., et al. 2019, *A&A*, 632, A122
- Marconi, A., Axon, D. J., Maiolino, R., et al. 2008, *ApJ*, 678, 2, 693
- Marian, V., Jahnke, K., Andika, I., et al. 2020, *ApJ*, 904, 79
- Marian, V., Jahnke, K., Mechtley, M., et al. 2019, *ApJ*, 882, 141
- Masters, K. L., Nichol, R. C., Haynes, M. P., et al. 2012, *MNRAS*, 424, 2180
- McAlpine, S., Harrison, C. M., Rosario, D. J., et al. 2020, *MNRAS*, 494, 5713
- Mechtley, M., Jahnke, K., Windhorst, R. A., et al. 2016, *ApJ*, 830, 156
- Mendel, J. T., Simard, L., Palmer, M., et al. 2014, *ApJS*, 210, 3
- Miller, C. J., Nichol, R. C., Reichart, D., et al. 2005, *AJ*, 130, 3, 968
- Oh, K., Yi, S. K., Schawinski, K., et al. 2015, *ApJS*, 219, 1
- Ohta, K., Aoki, K., Kawaguchi, T., et al. 2007, *ApJS*, 169, 1
- Osborne, C. & Salim, S. 2024, *ApJ*, 965, 161
- Panessa, F., Baldi, R. D., Laor, A., et al. 2019, *Nature Astronomy*, 3, 387
- Pierce, J. C. S., Tadhunter, C. N., Gordon, Y., et al. 2022, *MNRAS*, 510, 1, 1163
- Pierce, J. C. S., Tadhunter, C., Ramos Almeida, C., et al. 2023, *MNRAS*, 522, 1736
- Poggianti, B. M., Jaffé, Y. L., Moretti, A., et al. 2017, *Nature*, 548, 304
- Porter, S. C. & Raychaudhury, S. 2005, *MNRAS*, 364, 4, 1387
- Quinn, P. J. 1984, *ApJ*, 279, 596
- Sabater, J., Best, P. N., & Heckman, T. M. 2015, *MNRAS*, 447, 110
- Sacchi, A., Risaliti, G., Signorini, M., et al. 2022, *A&A*, 663, L7
- Schawinski, K., Dowlin, N., Thomas, D., et al. 2010, *ApJ*, 714, L108
- Schmitt, H. R., Donley, J. L., Antonucci, R. R. J., et al. 2003, *ApJ*, 597, 2, 768
- Schweizer, F. & Seitzer, P. 1992, *AJ*, 104, 1039
- Shah, E. A., Kartaltepe, J. S., Magagnoli, C. T., et al. 2020, *ApJ*, 904, 107
- Sheen, Y.-K., Yi, S. K., Ree, C. H., et al. 2012, *ApJS*, 202, 8
- Sheen, Y.-K., Yi, S. K., Ree, C. H., et al. 2016, *ApJ*, 827, 32
- Shlosman, I., Frank, J., & Begelman, M. C. 1989, *Nature*, 338, 45
- Simard, L., Mendel, J. T., Patton, D. R., et al. 2011, *ApJS*, 196, 11
- Sola, E., Duc, P.-A., Richards, F., et al. 2022, *A&A*, 662, A124
- Springel, V., Di Matteo, T., & Hernquist, L. 2005, *MNRAS*, 361, 776
- Steffen, J. L., Fu, H., Brownstein, J. R., et al. 2023, *ApJ*, 942, 107
- Steinborn, L. K., Hirschmann, M., Dolag, K., et al. 2018, *MNRAS*, 481, 341
- Tal, T., van Dokkum, P. G., Nelan, J., et al. 2009, *AJ*, 138, 1417
- Tang, S., Silverman, J. D., Yesuf, H. M., et al. 2023, *MNRAS*, 521, 5272
- Tempel, E., Tamm, A., Gramann, M., et al. 2014, *A&A*, 566, A1
- Treister, E., Schawinski, K., Urry, C. M., et al. 2012, *ApJ*, 758, L39
- Tremblay, G. R., Oonk, J. B. R., Combes, F., et al. 2016, *Nature*, 534, 218
- Urbano-Mayorgas, J. J., Villar Martín, M., Buitrago, F., et al. 2019, *MNRAS*, 483, 1829
- Urrutia, T., Lacy, M., & Becker, R. H. 2008, *ApJ*, 674, 80
- Urry, C. M. & Padovani, P. 1995, *PASP*, 107, 803
- Villforth, C., Hamann, F., Rosario, D. J., et al. 2014, *MNRAS*, 439, 3342
- Villforth, C., Hamilton, T., Pawlik, M. M., et al. 2017, *MNRAS*, 466, 812
- Wang, F., Yang, J., Fan, X., et al. 2021, *ApJ*, 907, L1
- Yoon, Y., Kim, J.-W., & Ko, J. 2024a, *ApJ*, 974, 299
- Yoon, Y., Ko, J., Chung, H., et al. 2024b, *ApJ*, 965, 158
- Yoon, Y., Ko, J., & Kim, J.-W. 2023, *ApJ*, 946, 41
- Yoon, Y. & Lim, G. 2020, *ApJ*, 905, 154
- Yoon, Y. & Park, C. 2020, *ApJ*, 897, 121
- Yoon, Y., Park, C., Chung, H., et al. 2022, *ApJ*, 925, 168
- Zhao, Y., Li, Y. A., Shangguan, J., et al. 2022, *ApJ*, 925, 70